Nanotechnology 32 (2021) 145702 (11pp)

Structural, optical, photocatalytic, and optoelectronic properties of Zn₂SnO₄ nanocrystals prepared by hydrothermal method

Yifang Qi¹, William E Meador², Jian Xiong¹, Mahsa Abbaszadeh³, Rooban Venkatesh K G Thirumala⁴, Jared H Delcamp², Santanu Kundu³, Glake Alton Hill Jr¹ and Qilin Dai^{1,*}

E-mail: qilin.dai@jsums.edu

Received 10 September 2020, revised 2 December 2020 Accepted for publication 18 December 2020 Published 11 January 2021



Abstract

Zn₂SnO₄ (ZTO) nanocrystals are extensively studied in various fields. However, size-dependent ZTO nanocrystals are still challenging to understand their structural, optical, photocatalytic, and optoelectronic properties. ZTO nanocrystals are synthesized by a facile hydrothermal reaction method. The structural properties of the synthesized ZTO nanocrystals are studied by x-ray diffraction and transmission electron microscope. The sizes of the ZTO nanocrystals are controlled by the pH values of the precursor and the molar ratios of the Zn:Sn in the starting materials. ZTO nanocrystals with the small size of 6 nm and large size of 270 nm are obtained by our method. The Eu³⁺ ions are doped into ZTO nanocrystals to probe size-dependent Eu doping sites, which shows significant potential applications in light emitting diode phosphors. Moreover, the photocatalytic activity of ZTO nanocrystals on rhodamine (RhB) decoloration are investigated, and the results show that 6 nm ZTO nanocrystals show better performance in the photocatalytic decoloration of RhB compared to 270 nm nanocrystals. Most importantly, we design and fabricate optoelectronic devices to detect IR light based on our nanocrystals and a self-prepared NIR cyanine dye. The device based on small sized ZTO nanocrystals exhibits better device performance under 808 nm IR light compared to that of the large sized ZTO nanocrystals. We believe this work represents ZTO size-dependent properties in term of structural, optical, photocatalytic, and optoelectronic properties as a multifunctional material.

Supplementary material for this article is available online

Keywords: Zn₂SnO₄, small sized, 6 nm, photocatalytic properties, optoelectronic properties

1

(Some figures may appear in colour only in the online journal)

¹ Department of Chemistry, Physics, and Atmospheric Sciences, Jackson State University, Jackson, MS, 39217, United States of America

² Department of Chemistry and Biochemistry, University of Mississippi, University, Mississippi 38677, United States of America

³ Dave C. Swalm School of Chemical Engineering, Mississippi State University, 323 Presidents Circle, Mississippi State, Mississippi, 39762, United States of America

⁴ Institute for Imaging & Analytical Technologies, Mississippi State University, 323 Presidents Circle, Mississippi State, Mississippi, 39762, United States of America

^{*} Author to whom any correspondence should be addressed.

1. Introduction

ZTO has attracted widespread attention due to its high electron mobility, high conductivity and wide band gap (3.6 eV) [1], and applications in light emitting diodes (LEDs), photocatalyst, and photovoltaics devices [2–7]. In recent years, many methods to synthesize ZTO nanocrystals are reported. Chen et al prepared ZTO nanowires with a diameter of about 100 nm by a chemical evaporation deposition method [8]. Jie et al controlled the diameters of ZTO nanowires to be 20-100 nm by a thermal evaporation of a mixture of ZnO and SnO₂ powders using gold as a catalyst [9]. ZTO nanocrystals with the sizes of 14 nm, 10 nm, 50 nm, and 1 μ m were prepared by sol-gel synthesis [10], chemical precipitation [11], high energy mechanical milling [12] and high temperature calcination [13], respectively. Intense research efforts are committed to synthesizing nanosized ZTO. The minimum size of ZTO nanocrystals is reported to be 10-30 nm with very broad size distribution [14]. The challenge of obtaining smaller sized ZTO nanocrystals (less than 10 nm) by reported methods remains. In addition, the properties affected by the nanocrystal sizes are attracting more interests since the smaller sized nanocrystals exhibit significant potential in additional applications compared to large sized nanocrystals in the fields of luminescence, photocatalysis, and optoelectronics. Therefore, the smaller sized ZTO nanocrystals are in high demand for the development of science and technology.

pH values and the ratios of the starting materials are critical experimental parameters to control the nanocrystal growth in terms of sizes and morphology with solution methods [15–23]. It is believed that pH values of the precursor affect the chemical potential of the reactions, and shift the reaction toward a lower energy path, leading to a morphology change [17]. The ratios of the starting materials influences the environment of nucleation and recrystallization, resulting in different sizes [15, 16, 20–22]. As an example, different sizes and morphologies of oBi₂S₃, ZnSe, Co₃(PO₄)₂ and TiO₂/CeO₂ were controlled by pH values and ratios of the starting materials [17, 20, 22, 24]. Therefore, pH values and the ratios of the starting materials exhibit significant potential in controlling the properties of synthesized ZTO nanocrystals.

ZTO may be an excellent photocatalysis candidate due to a high electrical conductivity and electron mobility [1, 2]. However, the inferior adsorption and fast recombination of the photogenerated electron-hole pairs in ZTO leads to poor photocatalytic activity [3, 6, 10, 11, 14]. The morphology and sizes of the nanocrystals are believed to influence the photocatalytic activity dramatically [24, 25]. Research efforts show that morphology control of ZTO nanocrystals could improve the photocatalytic activity of ZTO; however, the size-dependent photocatalytic activity measurements of ZTO nanocrystals are still challenging to obtain since the reported ZTO nanocrystal smaller sizes are limited to 10–30 nm [14]. Therefore, the investigations of smaller sized ZTO nanocrystal (less than 10 nm) photocatalytic activity is urgently necessary for the development of ZTO photocatalysts since

small sizes might exhibit significant potential toward improving the photocatalytic activity of ZTO.

ZTO with a similar band structure than TiO₂ is reported to be very promising with regard to electron collection in optoelectronic devices, such as solar cells, photodetectors, and LEDs [2-6]. It is generally accepted that ZTO offers more freedom in terms of energy level alignment than binary semiconductors such as the typical TiO₂ semiconductor, leading to improved electron collection and device performance in optoelectronic devices [2, 26, 27]. ZTO nanocrystals with a size of \sim 80 nm were studied in dye-sensitized solar cells by Wang and Wu groups [2, 26]. However, the cell performance was reported to be lower than that of TiO₂. Potentially, the size of 80 nm is not the optimal size for the ZTO-based devices, while it has been demonstrated that the size of \sim 20 nm is the optimized size for TiO₂-based devices [28]. Therefore, small sized ZTO nanocrystals might show better performance than that of TiO2. Thus, the research of size-dependent ZTO nanocrystals is needed to understand their charge transport properties.

In this work, the size of ZTO nanocrystals is controlled by adjusting pH and the molar ratios of Zn:Sn in the precursor solutions. Figure 1(a) shows the schematic of the synthesis process of ZTO nanocrystals in this work. ZnCl₂ reacts with SnCl₄ under alkaline conditions to form ZTO. Figures 1(b) and (c) shows the synthesis parameters of large sized and small sized ZTO nanocrystals controlled by different experimental conditions, respectively. ZTO nanocrystals with the sizes of 270 nm (S1) and 6 nm (S2) are obtained by our method. The structural, optical, photocatalytic, and optoelectronic properties of the large and small sized ZTO nanocrystals are investigated for comparation. We demonstrate that the small sized ZTO nanocrystals exhibit better performance including in photocatalysis and IR photodetector applications. This work demonstrates the advantages of the smaller ZTO nanocrystals in multiple applications over large nanocrystals.

2. Experimental methods

2.1. Chemical and materials

All chemicals were used as received. Zinc Chloride anhydrous (ZnCl $_2 \geqslant 98\%$) and Europium(III) nitrate hexahydrate (Eu(NO $_3$) $_3 \cdot 6H_2$ O) were purchased from Alfa-Aesar. Tertbutylamine ($\geqslant 99\%$), Tin Chloride (SnCl $_4 \geqslant 98\%$) and Rhodamine B (RhB) were purchased from Acros Organics. Ethylene Glycol ($\geqslant 99.9\%$) was purchased from Fisher Chemical. *N,N'*-dimethylformamide (DMF) (anhydrous, $\geqslant 99.8\%$) was purchased from Sigma-Aldrich. Fast Drying Silver Paint was purchased from TED PELLA, INC. PEDOT:PSS (AI 4083) was purchased from Ossila and Triton x-100 was purchased from VWR LIFE SCIENCE.

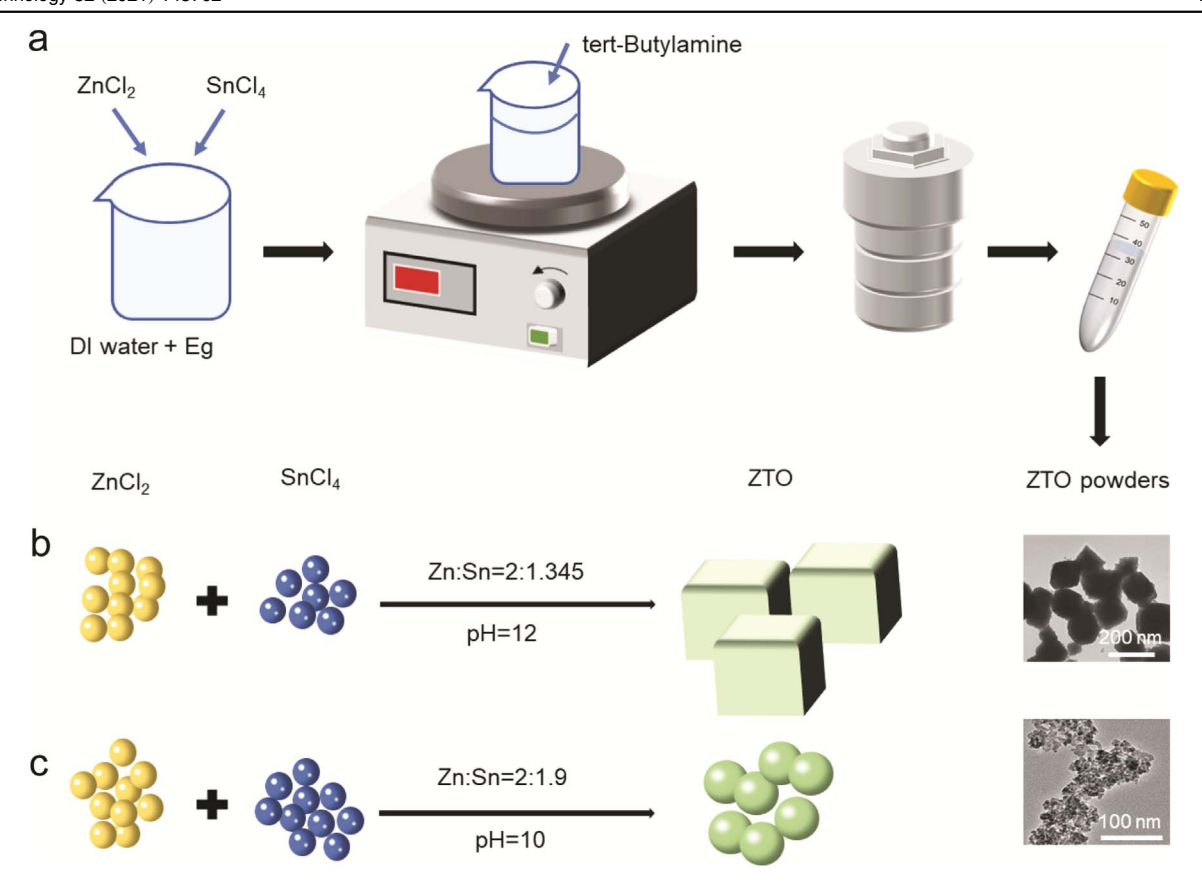


Figure 1. (a) Experimental procedure for ZTO nanoparticle synthesis using $ZnCl_2$ and $SnCl_4$ as starting materials by a hydrothermal method; (b) the synthetic route to S1 under the conditions of Zn:Sn=2:1.345 and pH=12; (c) the synthetic route to S2 under the conditions of Zn:Sn=2:1.9 and pH=10.

2.2. ZTO nanocrystal preparation

The ZTO nanocrystals were prepared by a hydrothermal method according to the literature [2]. The experimental procedure was modified as follows: 0.525 g zinc chloride anhydrous and 0.965 g tin chloride were dissolved in a 50 ml mixture of ethylene glycol and distilled water (1:1, v/v) and kept stirring. After stirring for 20 min, the pH values of the precursor solution were adjusted using the proper amount of tert-butylamine, which was added to the solution dropwise. After stirring for another 30 min, the obtained precursor solution was transferred to a 100 ml autoclave and kept at 180 °C for 24 h. Then the autoclave was cooled down to room temperature naturally. The precipitates in the autoclave were washed five times with distilled water and two times with ethanol to purify the samples. Finally, the powders were obtained by drying under vacuum at 60 °C for 6 h. Eu doped ZTO nanocrystals were prepared by a similar procedure. 0.017 g, 0.138 g, 0.173 g, and 0.26 g Eu(NO₃)₃ corresponds to 1%, 8%, 10% and 15% doping concentration (molar ratio of Eu:Zn) were added into the precursor solutions for the synthesis of Eu doped ZTO nanocrystals.

2.3. Photocatalysis test

ZTO powders were added into a 250 ml RhB aqueous solution (30 mg l^{-1}), and kept stirring for 15 min to allow for the

establishment of an adsorption–desorption equilibrium. Then UV light irradiation was introduced to the solution. The distance between the light source and the top of the solution was about 15 cm. At different time intervals, 4 ml solution was extracted by a syringe, and a filter (pore size 0.45 $\mu \rm m)$ was utilized to remove the ZTO particles in the dye solution. The filtrate was subsequently characterized by UV–vis absorption spectroscopy.

2.4. Photodetector device fabrication

1 g ZTO nanocrystals were dispersed in a mixture of 2 ml of anhydrous ethanol and 80 μ l Triton x-100, and kept stirring for 12 h. Then, 9 ml of anhydrous ethanol was added into the solution and kept stirring for another 48 h to obtain a ZTO paste. NIR indolizine-cyanine dye (C5)was synthesized as published previously [29], and was utilized as a light absorber in the photodetectors. 8 mg of C5 was dissolved in 1 ml DMF to obtain the NIR absorbing solution. FTO coated glass substrates were sequentially cleaned by an ultrasonic bath using deionized water, acetone, and ethanol for 15 min and followed by UV ozone treatment for 15 min 150 μ l ZTO paste was spin-coated on top of the cleaned FTO electrode at a spin speed of 2000 rpm for 30 s, followed by annealing at 400 °C for 1 h using a hotplate. 100 μ l of NIR dye solution was spincoated onto the top of ZTO at a spin speed of 1000 rpm for 30 s, followed by drying at 50 °C for 10 min using a hotplate

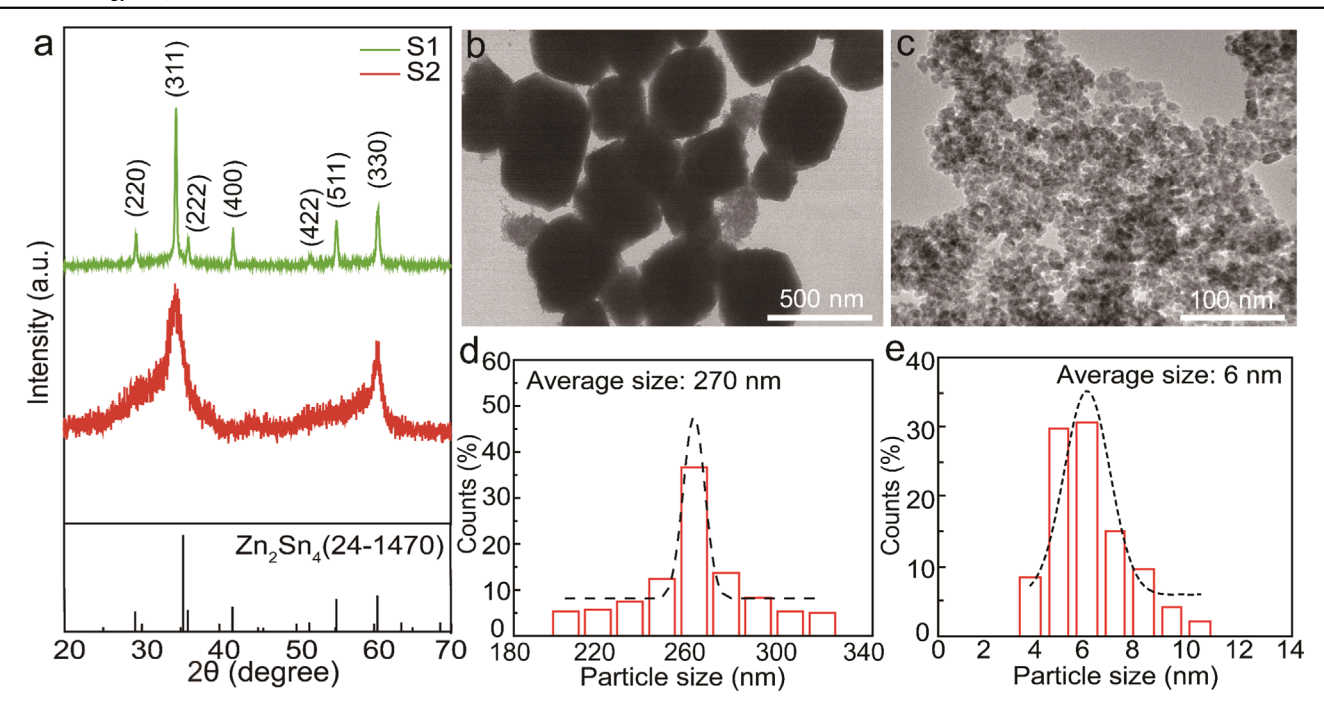


Figure 2. Structural characterizations of Zn_2SnO_4 (ZTO) (a) XRD data of S1 and S2; (b) TEM image of S1; (c) TEM image of S2; (d) size distribution of S1; (e) size distribution of S2.

to form a NIR dye film 200 μ l PEDOT:PSS was dropped-casted on top of the NIR dye film, followed by drying at 50 °C for 1 h with a hot plate. A silver film was prepared by a doctor blade technique with \sim 100 μ l of fast drying silver paint to finish the photodetector device fabrication.

2.5. Materials characterization

A MiniFlex600 (Rigaku) x-ray diffraction (XRD) diffractometer (Cu K α radiation source $\lambda = 1.54056$ Å) was used to study the phase of ZTO nanocrystals with 2-theta ranging from 20° to 70° and a step size of 5° min⁻¹ during data collection. Transmission electron microscope (TEM) images were obtained by a JEM-1011 TEM (JEOL) and a JEOL 2100 with energy dispersive x-ray spectroscopy (EDS) spectra system for elemental analysis and mapping. TEM was operated at 200 kV and samples were mounted on copper grids for TEM imaging. The photoluminescence (PL), PL excitation (PLE) and time resolved PL (TRPL) spectra were collected using a fluorescence spectrometer (FluoroMax, Horiba) with DeltaHub and NanoLED. BLAK-RAY Ultraviolet Lamp (Model B 100 AP) was utilized for the photocatalyst study. The UV-vis absorption spectra were measured by a Cary 60 UV-vis spectrophotometer (Agilent Technologies). The current-time properties of the photodetectors were collected using a digital source meter (2450, Keithley Instruments Inc.) under 808 nm laser irradiation (Civil Laser). The power of the laser was measured by an optical Power Meter (Newport 1930F-SL-FC Si Detector SC/PC).

3. Results and discussion

3.1. Structural properties

XRD diffraction patterns and TEM images are used to investigate the crystal phase properties and the morphology of the ZTO nanocrystals prepared with the different experimental parameters. Figure 2(a) shows the XRD results of ZTO nanocrystals S1 and S2. S1 was synthesized with a Zn: Sn molar ratio of 2:1.345 and a pH value of 12. S2 was prepared with a Zn:Sn molar ratio of 2:1.9 and pH value of 10. Both S1 and S2 show cubic inverse spinel phase (JCPDS No. 00-24-1470). The standard card is also listed in the figure for comparison. The XRD diffraction patterns of S1 exhibit sharp peaks compared to that of S2 indicating the large sizes and better crystallinity of S1. Diffraction peaks of (220), (222), (400), (422), (511) of S2 are not obvious, which can be attributed to weak crystallinity of the S2. Figures 2(b) and (c) show the TEM images of S1 and S2, respectively. Figures 2(d) and (e) show the size distribution histograms of S1 and S2, respectively. The average size of S1 is about 270 nm (figure 2(d)), while the average size of S2 is about 6 nm (figure 2(e)). The size of S2 is calculated to be about \sim 4 nm using Debye-Scherrer formula, which is comparable to the size obtained by TEM images. Figure S1 (available online at stacks.iop.org/NANO/32/145702/mmedia) shows the EDS element mapping images of S2, which confirms Zn, Sn and O elements in the nanocrystals. These three elements have a consistent distribution as expected. The element ratio of Zn to Sn is calculated to be \sim 2:1 by EDS measurement for S1 and S2 (figure S2). Different molar ratios of ZnCl₂ to SnCl₄ and pH values of the precursor are used to synthesize the ZTO nanocrystals. The molar ratios of Zn:Sn are 2:1.345, 2:1.445,

2:1.545, 2:1.645, 2:1.745, 2:1.9 and are selected to synthesize ZTO nanocrystals based on the results reported by Wu et al [2]. High-resolution transmission electron microscopy images and selected area electron diffraction patterns of S1 and S2 are shown in figure S3. The diffraction patterns are analyzed and labeled in the figure. Figure S4 shows XRD diffraction patterns of the ZTO nanocrystals prepared by the different molar ratios of Zn:Sn with pH value of 10. It can be observed that all the samples exhibit the cubic inverse-spinel phase [30]. All the crystal planes of the ZTO nanocrystals can be indexed into the cubic phase. The lack of additional phases produced in the samples indicates the success and consistency of our method. The full width at half maximum values of the diffraction peaks (311) increase as the ratios of Zn:Sn increase from 2:1.345 to 2:1.9. The pH values of the precursor solutions are controlled to be 10, 11 and 12 to control the synthesis of ZTO nanocrystals. Figure S5 shows the XRD diffraction patterns of the samples prepared by different pH values via controlling the amount of tert-butylamine with a constant Zn:Sn ratio of 2:1.345. All the nanocrystals present the same cubic crystal phase (JCPDS No. 00-24-1470), which is consistent with the results in figure S4. Therefore, ZTO nanocrystals can be synthesized by different Zn:Sn ratios and pH values of the precursor in the hydrothermal method used herein. Figure S6 shows the TEM images of the ZTO nanocrystals prepared with different Zn:Sn ratios (pH = 10). \sim 6 nm small nanocrystals (S2) and large nanocrystals (\sim 50 nm) are observed in figures S6(a)-(c) corresponding to Zn:Sn ratios of 2:1.345, 2:1.445, and 2:1.545. Only small nanocrystals are presented in figure S6(d). Thus, small nanocrystals are exhibited as the ratio of Zn:Sn increases from 2:1.345 to 2:1.9. This can be explained by the different chemical ratios of Zn:Sn during the nucleation process of the reactions which are affected by monomer consumption [17, 23]. The reaction toward large nanocrystals is possibly prohibited at the ratio of 2:1.9 Zn:Sn, which leads to small nanocrystal production. Figure S7 shows the TEM images of the ZTO nanocrystals prepared under the pH values of 10, 11 and 12 (Zn:Sn = 2:1.345). Both large and small nanocrystals are observed for the sample prepared with pH values of 10 and 11. Only large nanocrystals with the size of \sim 270 nm (S1) are observed as the pH value increases to 12, indicating that the larger pH values are integral to large nanocrystals. pH values may influence the recrystallization process toward large nanocrystals if the smaller nanocrystals are consumed in order to form large nanocrystals.

3.2. Optical properties

In order to study the influence of crystal size on the optical properties of ZTO nanocrystals, S1 and S2 are selected for Eu doping. Figures 3(a) and (b) show the PLE spectra of S1 and S2 with different Eu doping concentrations ($\lambda_{em} = 611$ nm), respectively. The peaks at ~ 393 nm and ~ 464 nm are ascribed to the $^7F_0-^5L_6$, and $^7F_0-^5D_2$ energy level transitions of the Eu³⁺, respectively [31]. In figure 3(a), a broad band at 370–450 nm is observed for S1, which is attributed to an absorption caused by defects in the ZTO matrix. The PL

spectrum of S1 doped with 10% Eu and excited with 398 nm (figure S8) corresponds to a broad band and confirms the energy transfer from ZTO to Eu. Dimitrievska et al reported the energy transfer from ZTO to Eu using ZTO particles prepared at 1200 °C for 2 h [31]. However, their study showed that the ZTO matrix absorption band peak was at 335 nm, which was attributed to matrix absorption and the chargetransfer transition band [31]. The inconsistency between our measurements and those previously reported can be attributed to the crystallinity of ZTO and Eu sites located in the ZTO matrix, which is associated with the preparation temperature and method. In figure 3(b), the sharp peaks at \sim 393 and \sim 464 nm in the PLE spectra of S2 dominate the PLE spectra compared to that of S1 as shown in figure 3(a), indicating that the relative absorption intensity of Eu itself (${}^{7}F_{0}-{}^{5}L_{6}$, and ⁷F₀-⁵D₂) increases with the decreasing sizes of ZTO nanocrystals. Smaller nanocrystals would demonstrate larger surface-area-to-volume ratios compared to larger nanocrystals, leading to more Eu doping sites located on the surface of the small nanocrystals [32]. It is reported that energy transfer efficiency decreases for the case of surface doping compared to interior doping due to the disordered surface environments of the small nanocrystals [32-34], which also explains the decreased intensity of the broad band (370-450 nm) in figure 3(b) compared to figure 3(a). S2 with a doping concentration of 15% Eu in figure 3(b) exhibits a weak broad band due to high concentration doping, which leads to more interior doping compared to low concentration samples (8% and 10%). Figure 3(c) shows the PLE spectra of S2 doped with 10% Eu annealed at different temperatures. The broad band (370–450 nm) appears with the annealing temperature at 900 °C compared to samples annealed at 300 °C and the unannealed. The small nanocrystals aggregate to form large nanocrystals, and Eu ions immigrate into the large nanocrystal inner sites during the high temperature annealing (900 °C), leading to increased interior doping and the relative efficient energy transfer from ZTO to Eu. Thus, the broad band (370–450 nm) is observed with high temperature sample annealing. Note that the relative excitation peak intensity at 464 nm increases substantially with increasing annealing temperatures, which shows significant potential in LED phosphors [34, 35]. The PL spectrum of S2 doped with 10% Eu under the excitation of 464 nm is shown in figure 3(d). The peaks at 578, 595, 611 and 650 nm are attributed to ${}^{5}D_{0} - {}^{7}F_{0}$, ${}^{5}D_{0} - {}^{7}F_{1}$, ${}^{5}D_{0} - {}^{7}F_{2}$ and ${}^{5}D_{0} - {}^{7}F_{3}$ energy level transitions of Eu³⁺, respectively. Figure S9 shows the PLE spectra of 10% Eu doped S1 annealed at different temperatures, all of which are similar to one another. The relative excitation peak intensity at 464 nm also increases dramatically with increasing annealing temperatures, which is consistent with figure 3(c). Figures S9(b) and (c) show PL spectra of 10% Eu doped S1 and S2 annealed at different temperatures with excitation at 393 nm. Emission peaks at 578, 595 and 611 nm become obvious as the annealing temperature increases to 900 °C, which can be explained by the increased crystallinity caused by the higher temperature annealing. Figure S9(d) is the PL spectra of 10% Eu doped S2 annealed at 600 °C and 900 °C, which show similar features compared

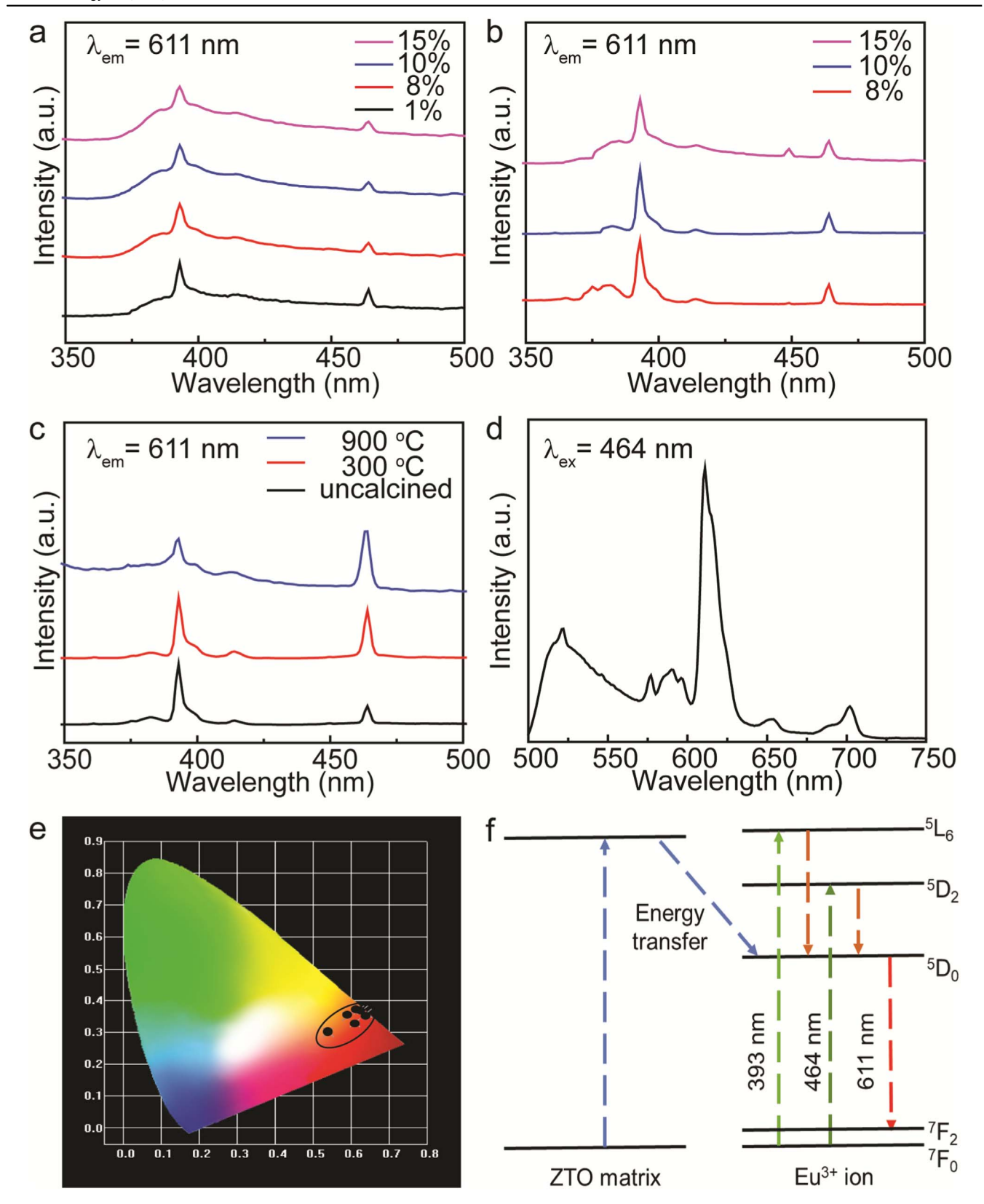


Figure 3. (a) PLE spectra of Eu doped S1; (b) PLE spectra of Eu doped S2 nanocrystals; (c) PLE spectra of Eu doped S2 after annealing 300 °C and 900 °C; (d) PL spectra of Eu doped S2; (e) the CIE coordinates of Eu doped S1 and S2 based on the PL in figure S9; (f) PL schematic of electron pumping and relaxation pathways in ZTO:Eu nanocrystals.

to figure 3(d). Figures S9(e) and (f) exhibit PL spectra of S1 and S2 doped with different Eu concentrations under the excitation of 393 nm, which look identical. The International Commission on Illumination (CIE) coordinates based on the PL spectra in figure S9 are shown in figure 3(e). The observed coordinates are in the red and orange regions. This also shows the feasibility of ZTO:Eu nanocrystals in UV-LED and LED phosphor applications [35-39]. Figure 3(f) shows the PL schematic of electron pumping and relaxation pathways in ZTO:Eu nanocrystals. The ZTO matrix absorbs light due to defects in the crystallinity and energy transfer to Eu³⁺ leading to red emission of Eu^{3+} due to ${}^5D_0-{}^7F_j$ transitions. Meanwhile, the intrinsic absorption of Eu3+ itself is due to the $^{7}F_{0}$ – $^{5}L_{6}$, and $^{7}F_{0}$ – $^{5}D_{2}$ transitions at 393 and 464 nm which can also populate the ${}^{5}D_{0}$ energy levels for ${}^{5}D_{0}-{}^{7}F_{i}$ transitions. According to figures 3(a) and (b), the sizes of ZTO nanocrystals can control the PL mechanisms in terms of energy absorption and transfer, leading to the potential applications in LED phosphors.

3.3. Photocatalytic properties

Size-dependent photocatalytic performances of ZTO nanocrystals for RhB decoloration are investigated and shown in figure 4. Figure 4(a) shows the mechanism of photocatalysis properties of the ZTO nanocrystals in terms of RhB decoloration. Electrons in the valance band (VB) of ZTO will transition to the conduction band (CB) under ultraviolet radiation, generating holes in the VB. The electrons in the CB and holes in the VB may then migrate to the surface of ZTO, where the electrons reduce $\rm O_2$ and $\rm H_2O$ to hydroxyl radicals, and the holes oxidize $\rm OH^-$ to hydroxyl radicals.

The produced hydroxyl radicals decolor RhB to produce CO_2 and H_2O [40]. The inset in figure 4(a) shows the molecular structure of RhB [41]. The CB and VB positions in figure 4(a) is based on that reported in the literature [2]. The RhB solution decoloration without ZTO under UV irradiation 0 min and 60 min in figure S10 suggests RhB solution decoloration by UV light is not obvious, which can be neglected. Figure S11 shows the effects of ZTO amount on RhB decoloration (a S1, b S2) after 60 min of treatment. The UV-vis absorption spectra show the 553 nm and 515 nm absorption features of RhB. The curve labeled with 0 g shows the original RhB absorption without any ZTO treatment. The absorption peak intensity decreases with increasing ZTO amount due to effective RhB decoloration caused by the photocatalysis properties of ZTO. Figures S12 and S13 show the influence of ZTO mass and UV light irradiation time of RhB decoloration for S1 and S2, respectively. Figures 4(b) and (c) show amount dependent ZTO photocatalytic activity (b S1, c S2). The dye decoloration degree (C/C_0) is influenced by the UV light irradiation time. C_0 is the RhB concentration before UV light. C is the RhB concentration under UV light irradiation as a function of time (t). The decoloration efficiency of RhB increases with increasing UV light irradiation time for both S1 and S2 samples. In figure 4(b), 0.2 g S1 ZTO nanocrystals show better photocatalytic activity than that of 0.05, 0.10 and 0.15 g ZTO. The decoloration efficiency increases as the amount of photocatalyst increases. More hydroxyl radicals are produced as the amount ZTO increases from 0.05 to 0.20 g. The same trend is also observed for S2 (figure 4(c)). Figures 4(d) and (e) shows the size-dependent photocatalytic activity of ZTO nanocrystals. The decoloration efficiency increases to 37.4% as the mass of ZTO increases to 0.2 g for S2, which shows better photocatalytic performances than that of S1 (29.2%). This can be explained by the larger surface area of S2 compared to S1 due to the small size of S2 [42].

3.4. Optoelectronic properties

Photodetectors based on the ZTO nanocrystals and C5 are fabricated to investigate the electron transport properties of ZTO. Figure 5(a) shows the vis-NIR absorption and PL spectra of C5 in DMF solution. The absorption ranges from 600 to 890 nm with a peak at 820 nm, which is interesting to explore for NIR photoresponse applications. The PL peak is located at 830 nm, which confirms a significant Stokes shift [29]. The inset in figure 5(a) shows the molecular structure of C5. Figure S14 shows the TRPL spectrum of C5 measured in DMF. The PL decay time constant is fitted to be 1.03 ns. Figure 5(b) shows the structure of our photodetector devices. ZTO nanocrystals, C5, and PEDOT: PSS are used as electron transport layer, light absorption layer, and hole transport layer, respectively. Figure 5(c) shows the device working principle, and energy level alignment of the layers in the devices. NIR light is absorbed by the dye molecules to generate electron-hole pairs. The photogenerated electrons are injected into the CB in ZTO. Then, the electrons are transported to FTO. The holes will be transferred to the PEDOT: PSS layer. Then, the holes are collected by the Ag contact. The photocurrent generated by the devices can then be detected. The energy levels of FTO, ZTO, C5, PEDOT:PSS and Ag are obtained from the literature [2, 29, 43–45]. Figure 5(d) shows the performance of the devices based on S1 and S2 with ZTO nanocrystals under 808 nm NIR light irradiation with a power of 1.852 W cm⁻². Obvious photocurrent on and off curves are observed in the figure 5. It can be seen that the 2.01 μA photocurrent is detected for the device based on S2, compared to that of 0.76 μ A for the S1 device. The on-off ratio values of the devices based on S1 and S2 are 7.5 and 12.5 under 1.852 W cm⁻² irradiation power, respectively. The performance of devices containing S2 is significantly better than those containing S1, which is attributed to the relative high quality of the films prepared with S2 in terms of surface smoothness. In addition, no photoresponse is observed for the devices without C5 or ZTO, which confirms the origin of the photocurrent is from the dye molecules. Figure 5(e) shows the dependence of S1 device performance on the IR light power. The photocurrent increases from 0.571 to 0.852 μ A as the light power increase from 0.571 to 1.852 W cm⁻². The same trend is also observed for the S2 devices (figure 5(f)), as the photocurrent increases from 0.64 to 2.01 μ A as the light power increase from 0.571 $1.852\,\mathrm{W\,cm^{-2}}$. Thus, more electron-hole pairs are

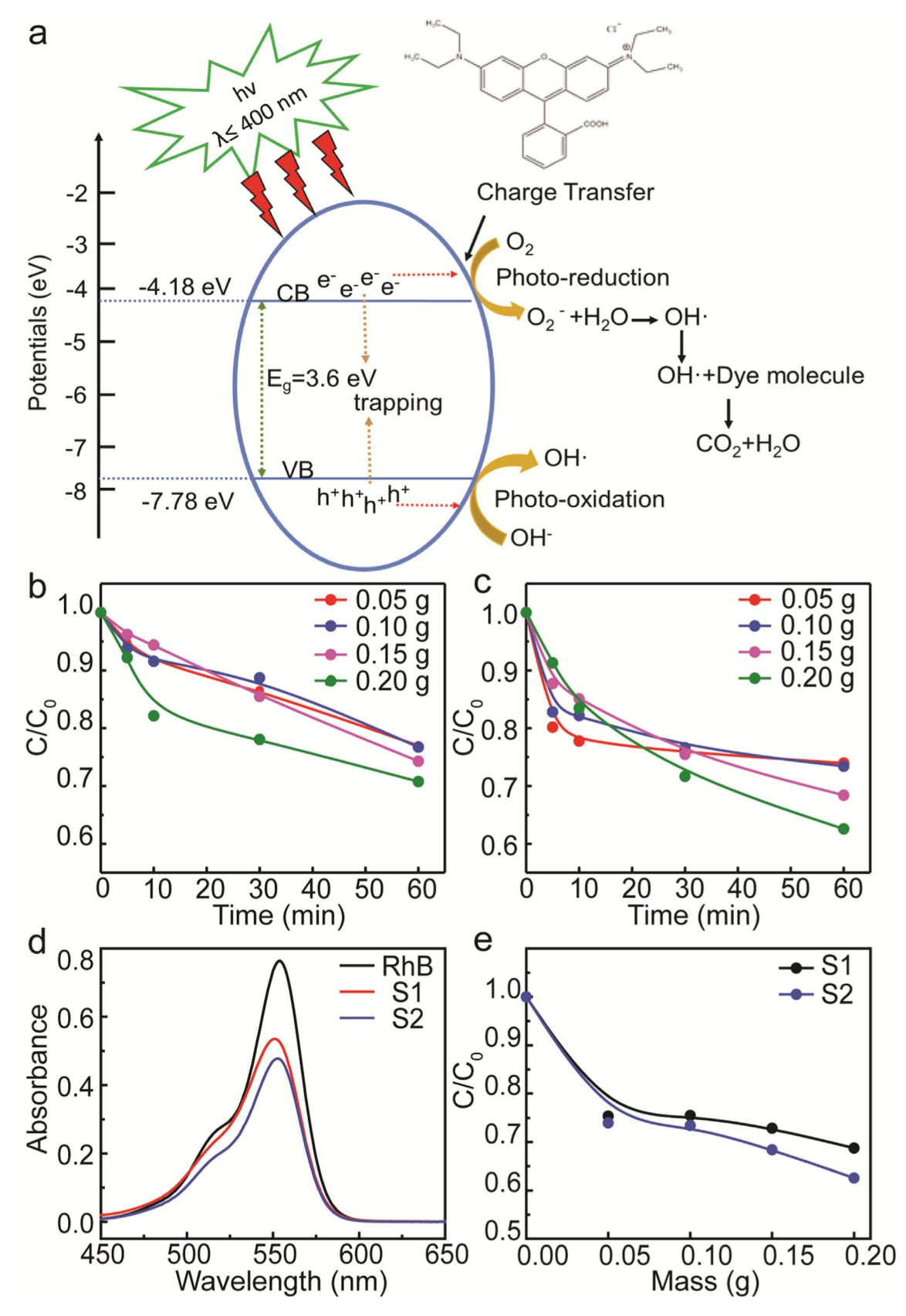


Figure 4. (a) The mechanism of photocatalysis with the ZTO nanocrystals in terms of RhB decoloration; (b) plotted graph of C/C_0 versus time with different amounts of S1 nanocrystals; (c) plotted graph of C/C_0 versus time with different amounts of S2 nanocrystals; (d) the UV–vis absorption spectra of RhB treated with 0.2 g S1 or S2 and UV light irradiation for 60 min; (e) plotted graph of C/C_0 versus different amounts of S1 and S2 nanocrystals with UV light irradiation for 60 min.

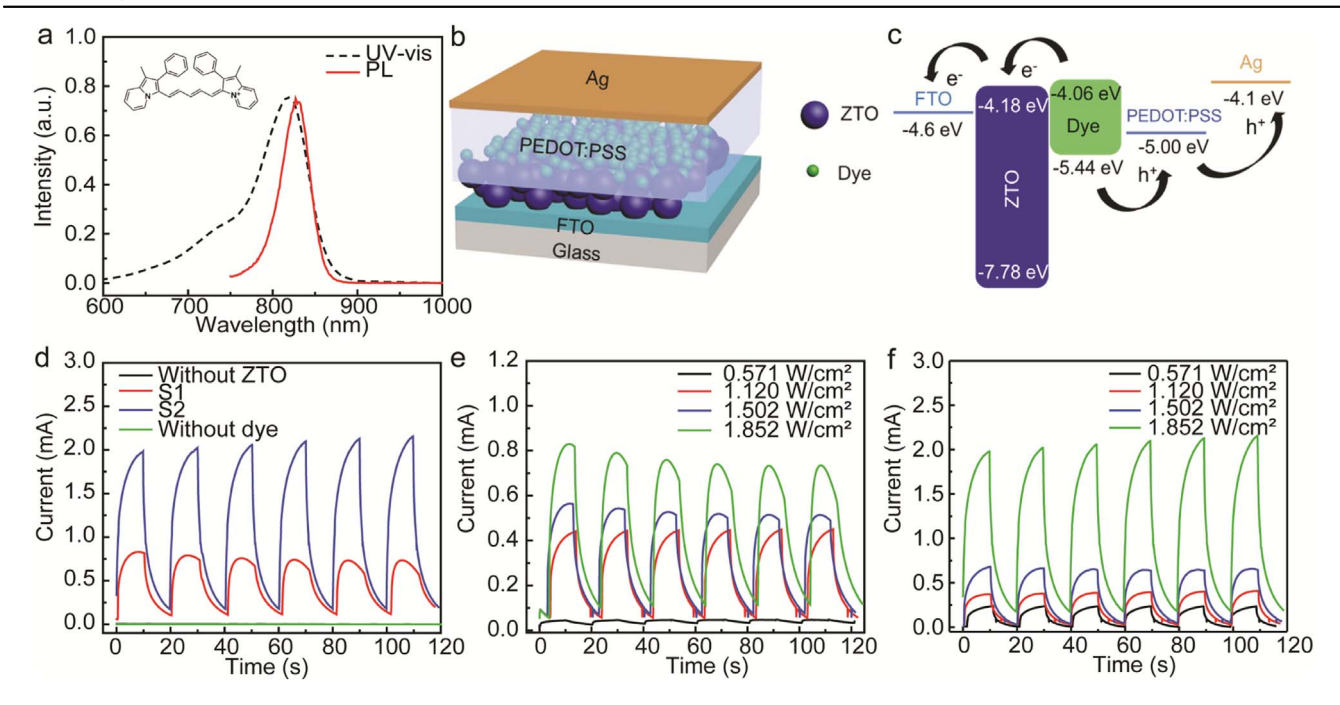


Figure 5. (a) The structure, UV–visible absorption, and PL spectra of C5; (b) the structure of photodetector devices; (c) the device working principle and energy level alignment of the layers in the devices; (d) performance of the devices based on S1 and S2 under the 808 nm IR irradiation with a light power of 1.86 W cm⁻²; (e) and (f) show the dependence of S1 and S2 device performance on the IR light power, respectively.

generated as the IR light power increases, leading to a larger photocurrent.

4. Conclusions

ZTO nanocrystals were synthesized with different sizes (\sim 6 and \sim 270 nm) by a hydrothermal method. The sizes of the ZTO nanocrystals decreases as the molar ratio of Zn:Sn approaches 1:1 in the starting materials, and the sizes of the ZTO nanocrystals increases with increasing pH values of the precursor solution. The size-dependent structural, optical, photocatalytic and optoelectronic properties are studied for comparison. Eu3+ luminescence in ZTO nanocrystals indicates that the energy transfer can be controlled by the ZTO sizes due to different Eu sites in the ZTO nanocrystals. Photocatalytic properties of the ZTO nanocrystals on RhB decoloration shows that small sized ZTO nanocrystals exhibit better performance due to a larger surface area. IR photodetectors are designed, fabricated and studied based on ZTO nanocrystals and NIR dye, C5. The devices based on S2 show better performance than that of S1, which can be explained by the quality of the S2 films increasing with smaller sizes nanoparticle sizes. This work represents the multifunctional aspect of ZTO nanocrystals in terms of LED phosphors, photocatalysts and photodetectors.

Acknowledgments

This material is based on work supported by the National Science Foundation under Grant No. 1757220. The steady

state PL and TRPL equipment used in this work is supported by National Science Foundation Research Initiation Award: Novel Perovskite Solar Cells Based on Interface Manipulation (Award#1900047).

ORCID iDs

Yifang Qi https://orcid.org/0000-0003-1748-4892 Qilin Dai https://orcid.org/0000-0001-8680-4306

References

- [1] Alpuche-Aviles M A and Wu Y 2009 Photoelectrochemical study of the band structure of Zn₂SnO₄ prepared by the hydrothermal method J. Am. Chem. Soc. 131 3216–24
- [2] Tan B, Toman E, Li Y and Wu Y 2007 Zinc stannate (Zn₂SnO₄) dye-sensitized solar cells *J. Am. Chem. Soc.* **129** 4162–3
- [3] Al-Attafi K, Jawdat F H, Qutaish H, Hayes P, Al-Keisy A, Shim K, Yamauchi Y, Dou S X, Nattestad A and Kim J H 2019 Cubic aggregates of Zn₂SnO₄ nanoparticles and their application in dye-sensitized solar cells *Nano Energy* 57 202–13
- [4] Zhao Q, Ju D, Song X, Deng X, Ding M, Xu X and Zeng H 2016 Polyhedral Zn₂SnO₄: synthesis, enhanced gas sensing and photocatalytic performance Sensors Actuators B 229 627–34
- [5] Vien L T T, Tu N, Viet D X, Anh D D, Nguyen D H and Huy P T 2020 Mn²⁺-doped Zn₂SnO₄ green phosphor for WLED applications J. Lumin. 227 117522
- [6] Samuel E, Kim T G, Park C W, Joshi B N and Yoon S S 2019 Supersonically sprayed Zn₂SnO₄/SnO₂/CNT

- nanocomposites for high-performance supercapacitor electrodes ACS Sustain. Chem. Eng. 7 14031–40
- [7] Ben Ali M, Barka-Bouaifel F, Elhouichet H, Sieber B, Addad A, Boussekey L, Férid M and Boukherroub R 2015 Hydrothermal synthesis, phase structure, optical and photocatalytic properties of Zn₂SnO₄ nanoparticles J. Colloid Interface Sci. 457 360–9
- [8] Chen H, Wang J, Yu H, Yang H, Xie S and Li J 2005 Transmission electron microscopy study of pseudoperiodically twinned Zn₂SnO₄ nanowires *J. Phys. Chem.* B 109 2573–7
- [9] Jie W, Wang H, Fang Y, Liao Y, Xu B, Wang W and Hou J G 2004 Growth of ternary oxide nanowires by gold-catalyzed vapor-phase evaporation J. Phys. Chem. B 108 8249–53
- [10] Xu W, Zheng L, Zhu T, Liu L and Gong X 2019 Bulk heterojunction perovskite solar cells incorporated with Zn₂SnO₄ nanoparticles as the electron acceptors ACS Appl. Mater. Interfaces 11 34020-9
- [11] Dou J, Shen D, Li Y, Abate A and Wei M 2019 Highly efficient perovskite solar cells based on a Zn₂SnO₄ compact layer ACS Appl. Mater. Interfaces 11 36553–9
- [12] Fakhrzad M, Navidpour A H, Tahari M and Abbasi S 2019 Synthesis of Zn₂SnO₄ nanoparticles used for photocatalytic purposes *Mater. Res. Express* 6 095037
- [13] Dimitrievska M, Ivetić T B, Litvinchuk A P, Fairbrother A, Miljevi B B, Štrbac G R, Rodríguez A P and Lukić-Petrović S R 2016 Eu³⁺ doped wide band gap Zn₂SnO₄ semiconductor nanoparticles: structure and luminescence *J. Phys. Chem.* C 120 18887–94
- [14] Zheng M, Xu W, Yuan H C and Wu J 2020 Mesostructured perovskite solar cells based on Zn₂SnO₄ single crystal mesoporous layer with efficiency of 18.32% *J. Alloys Compd.* 823 153730
- [15] Tsuji M, Hashimoto M, Nishizawa Y and Tsuji M K T 2004 Microwave-assisted synthesis of metallic nanostructures in solution *Chem. Eur. J.* 11 440–52
- [16] Salavati-Niasari M, Ghanbari D and Davar F 2009 Synthesis of different morphologies of bismuth sulfide nanostructures via hydrothermal process in the presence of thioglycolic acid *J. Alloys Compd.* 488 442–7
- [17] Mohammadi M R and Fray D J 2010 Nanostructured TiO₂-CeO₂ mixed oxides by an aqueous sol-gel process: effect of Ce:Ti molar ratio on physical and sensing properties Sensors Actuators B 150 631-40
- [18] Zeng J, Xin M D, Li K W, Wang H, Yan H and Zhang W J 2008 Transformation process and photocatalytic activities of hydrothermally synthesized Zn₂SnO₄ nanocrystals *J. Phys. Chem.* C 112 4159–67
- [19] An D, Mao N, Deng G, Zou Y, Li Y, Wei T and Lian X 2016 Ethanol gas-sensing characteristic of the Zn₂SnO₄ nanospheres Ceram. Int. 42 3535-41
- [20] Xing Y, Li M, Davis S A, Patila A J and Mann S 2006 Synthesis of cerium/cobalt phosphate nanostructures in catanionic reverse micelles Soft Matter 2 603–7
- [21] Wang X, Feng Z, Fan D, Fan F and Li C 2010 Shapecontrolled synthesis of CdS nanostructures via a solvothermal method *Cryst. Growth Des.* 10 5312–8
- [22] Tabar M B, Elahi S M, Ghorannevissa M and Yousefi R 2018 Controlled morphology of ZnSe nanostructures by varying Zn/Se molar ratio: the effects of different morphologies on optical properties and photocatalytic performance CrystEngComm 20 4590-9
- [23] Rong A, Gao X P, Li G R, Yan T Y, Zhu H Y, Qu J Q and Song D Y 2006 Hydrothermal synthesis of Zn_2SnO_4 as anode materials for Li-ion battery *J. Phys. Chem.* B **110** 14754–60
- [24] Lee J, Shim H S, Lee M, Song J K and Lee D 2011 Sizecontrolled electron transfer and photocatalytic activity of

- ZnO-Au nanoparticle composites *J. Phys. Chem. Lett.* **2** 2840-5
- [25] Cheng J, Chen J, Lin W, Liu Y and Kong Y 2015 Improved visible light photocatalytic activity of fluorine and nitrogen co-doped TiO₂ with tunable nanoparticle size *Appl. Surf.* Sci. 332 573–80
- [26] Chen J, Lu L and Wang W 2012 Zn₂SnO₄ nanowires as photoanode for dye-sensitized solar cells and the improvement on open-circuit voltage *J. Phys. Chem.* C 116 10841–7
- [27] Dai Q, Chen J, Lu L, Tang J and Wang W 2012 Pulsed laser deposition of CdSe quantum dots on Zn₂SnO₄ nanowires and their photovoltaic applications *Nano Lett.* 12 4187–93
- [28] Zhou C et al 2011 Titanium dioxide sols synthesized by hydrothermal methods using tetrabutyl titanate as starting material and the application in dye sensitized solar cells Electrochim. Acta 56 4308–14
- [29] Gayton J, Autry S A, Meador W, Parkin S R, Hill G A, Hammer N I and Delcamp J H 2019 Indolizine-cyanine dyes: near infrared emissive cyanine dyes with increased stokes shifts J. Org. Chem. 84 687–97
- [30] Habibi M H and Mardani M 2017 Synthesis and characterization of bi-component ZnSnO₃/Zn₂SnO₄ (perovskite/spinel) nano-composites for photocatalytic degradation of intracron blue: structural, opto-electronic and morphology study *J. Mol. Liq.* 238 397–401
- [31] Dimitrievska M, Ivetić T B, Litvinchuk A P, Fairbrother A, Miljević B B, Štrbac G R, Pérez Rodríguez A and Lukić-Petrović S R 2016 Eu³⁺-doped wide band gap Zn₂SnO₄ semiconductor nanoparticles: structure and luminescence *J. Phys. Chem.* C 120 18887–94
- [32] Lehmann O, Kömpe K and Haase M 2004 Synthesis of Eu³⁺-doped core and core/shell nanoparticles and direct spectroscopic identification of dopant sites at the surface and in the interior of the particles *J. Am. Chem. Soc.* 126 14935–42
- [33] Dai Q, Song H, Bai X, Pan G, Lu S, Wang T, Ren X and Zhao H 2007 Photoluminescence properties of ZnWO₄:Eu³⁺ nanocrystals prepared by a hydrothermal method *J. Phys. Chem.* C 111 7586–92
- [34] Dai Q, Foley M E, Breshike C J, Lita A and Strouse G F 2011 Ligand-passivated Eu:Y₂O₃ nanocrystals as a phosphor for white light emitting diodes J. Am. Chem. Soc. 133 15475–86
- [35] Zhou L-Y, Wei J-S, Gong F-Z, Huang J-L and Yi L-H 2008 A potential red phosphor ZnMoO₄:Eu³⁺ for light-emitting diode application *J. Solid State Chem.* **181** 1337–41
- [36] Xia M, Wu X, Zhong Y, Hintzen H T (Bert), Zhou Z and Wang J 2019 Photoluminescence properties and energy transfer in a novel Sr₈ZnY(PO₄)₇:Tb³⁺,Eu³⁺ phosphor with high thermal stability and its great potential for application in warm white light emitting diodes *J. Mater. Chem.* C 7 2977–35
- [37] Yi L, He X, Zhou L, Gong F, Wang R and Sun J 2010 A potential red phosphor LiGd(MoO₄)₂:Eu³⁺ for light-emitting diode application *J. Lumin.* 130 1113–7
- [38] Kim T-K, Kim T, Cha Y and Zoh K-D 2020 Energy-efficient erythromycin degradation using UV-LED (275 nm)/ chlorine process: radical contribution, transformation products, and toxicity evaluation *Water Res.* 185 116159
- [39] Xu X, Shao Q, Yao L, Dong Y and Jiang J 2020 Highly efficient and thermally stable Cr³⁺-activated silicate phosphors for broadband near-infrared LED applications *Chem. Eng. J.* 383 123108
- [40] Feng Z, Zeng L, Chen Y, Ma Y, Zhao C, Jin R, Lu Y, Wu Y and He Y 2017 *In situ* preparation of Z-scheme MoO₃/g-C₃N₄ composite with high performance in photocatalytic CO₂ reduction and RhB degradation *J. Mater.* Res. 32 3660–8

- [41] AlHamedi F H, Rauf M A and Ashraf S S 2009 Degradation studies of Rhodamine B in the presence of UV/H₂O₂ Desalination 239 159–66
- [42] Oh S H, Heo S J, Yang J S and Kim H J 2013 Effects of ZnO nanoparticles on P3HT:PCBM organic solar cells with DMF-modulated PEDOT:PSS buffer layers ACS Appl. Mater. Interfaces 5 11530–4
- [43] Zhao G, Kozuka H and Yoko T 1997 Effects of the incorporation of silver and gold nanoparticles on the
- photoanodic properties of rose bengal sensitized TiO_2 film electrodes prepared by sol-gel method *Sol. Energy Mater. Sol. Cells* **46** 219–31
- [44] Turrión M, Bisquert J and Salvador P 2003 Flatband potential of F: SnO_2 in a TiO_2 dye-sensitized solar cell: an interference reflection study *J. Phys. Chem.* B **107** 9397–403
- [45] Holzwarth U and Gibson Anon N 2011 The Scherrer equation versus the Debye–Scherrer equation *Nat. Nanotechnol.* 6 534